Effect of magnetic domain-wall curvature on velocity in the creep regime

Adriano Di Pietro,[*] Alessandro Magni, Gianfranco Durin, and Michaela Kuepferling
Istituto Nazionale di Ricerca Metrologica, Torino 10135, Italy

Giovanni Carlotti and Marco Madami
Dipartimento di Fisica e Geologia, Università di Perugia, Perugia 06123, Italy

Cristopher Marrows, Alexandra Huxtable, and Bryan Hickey
School of Physics and Astronomy, University of Leeds, Leeds LS2 9JT, United Kingdom

Silvia Tacchi
CNR-IOM, Sede Secondaria di Perugia, c/o Dipartimento di Fisica e Geologia, Università di Perugia,
I-06123 Perugia, Italy

Emily Darwin
Magnetic & Functional Thin Films Laboratory, Empa, Swiss Federal Laboratories for Materials Science and
Technology, 8600 Dübendorf, Switzerland

(Received 14 March 2025; revised 18 June 2025; accepted 30 June 2025; published 19 August 2025)

We study the effect of magnetic domain wall curvature on its dynamics in the creep regime in systems displaying Dzyaloshinskii-Moriya interaction (DMI). We first derive an extended creep model that is able to account for the finite curvature effect in magnetic bubble domain expansion. We then discuss the relative importance of this effect and discuss its dependence on the main magnetic and disorder parameters. We show this effect can be easily measured in Pt/Co multilayer samples, reporting a strong velocity reduction below a sample-dependent threshold value of the magnetic bubble radius. We finally show, both theoretically and experimentally, how the radius of magnetic bubbles can have a strong impact on the reproducibility of DMI measurements.

DOI: 10.1103/fh8q-7m45

I. INTRODUCTION

Magnetic domain wall (DW) motion in ferromagnetic thin films is a complex phenomenon displaying a variety of dynamical regimes, identified as creep, depinning, steady flow, and precessional flow [1–4]. Depending on which regime we are accessing, the measurement of the DW velocity in response to externally applied fields allows us to extract some key magnetic parameters of the sample. Among these magnetic parameters is the Dzyaloshinskii-Moriya interaction (DMI) [5,6] strength, which is becoming increasingly relevant because it can enhance the potential functionality of magnetic materials: we mention the stabilization of skyrmions [7–10] as potential information carriers for in-memory computing platforms, as well as enhanced DW velocity, useful to increase the performances of magnetic racetrack memory devices [11]. Measuring the DW velocity in the creep regime has the advantage of being possible under very easily accessible experimental conditions (low fields, long pulse duration, room temperature), but lacks a unified model relating the DW velocity to the magnetic properties of the sample [12–15]. The measurement of DMI strength via DW velocity methods in the creep regime [15–17] is a clear example of the need for more accurate models, as there have been accounts of large discrepancies in the reported DMI strength values, especially when comparing these values with those obtained via Brillouin light scattering (BLS) [13] or other disorder-independent methods (such as measurements in the flow regime) [18]. One factor that has seldom been inspected in the modeling of DW dynamics in the creep regime is the curvature of the DW [19–22]. In this paper, we address this issue by investigating the DW dynamics of magnetic bubble domains, taking into account the initial radius of the nucleated bubble. We demonstrate that the size of the circular magnetic domain in the creep regime can play a significant role in determining the

---

[*] Contact author: a.dipietro@inrim.it

speed of the magnetic domain wall. As a consequence, all the associated properties that are measured on the basis of the creep velocity require a precise knowledge of the initial bubble radius. In particular, we show how the consideration of a finite radius of the magnetic bubble can have very important consequences on the reproducibility of measurements of the DMI strength.

The paper is organized as follows: In Sec. II, we introduce the theoretical models describing magnetic bubbles and provide a brief overview of the theory of magnetic DW motion in the thermally activated (creep) regime. In Sec. II A we propose an extension of the creep model, which accounts for the DW curvature radius within the rigid bubble approximation. In Sec. III we report the model predictions, discussing which parameters are expected to have a greater impact on the relevance of the effect. In Sec. IV we provide experimental details regarding the measurement techniques, the sample characteristics, and the data analysis methods used to extract the DW velocities. In Sec. IV B we present our experimental results and show how our model can interpret the experimentally measured decreased DW velocity for small bubbles. We subsequently demonstrate how the incorporation of the bubble radius in the DW velocity model can improve the reproducibility of DMI measurements when dealing with bubbles with variable sizes. Finally, in Sec. V, we provide our conclusions and an outlook on future explorations regarding the radius dependence of the DW velocity.

II. THEORETICAL BACKGROUND

As mentioned in the Introduction (Sec. I), the dynamics of a magnetic DW under an applied out-of-plane (OOP) field displays several distinct regimes [23,24]. While the flow regime (and beyond) can effectively be described without taking into account the disorder potential [25,26] in which the magnetic domain wall moves, in the creep regime the DW follows an Arrhenius-type law [27], $v \propto \exp(-F_b/k_B T)$, where the velocity is determined by the competition between the energy barrier F_b imposed by the pinning potential and the thermal energy $k_B T$ (k_B representing the Boltzmann constant and T the temperature in Kelvin, see Appendix B). When a driving force f such as an applied OOP magnetic field is applied, the energy barrier scales with the creep power law $F_b \propto f^{-\mu}$, where μ is the creep critical exponent that depends on fundamental properties of the system such as its dimensionality and the range of interactions [23]. In typical ferromagnetic thin films, the value of the creep critical exponent is $\mu = 1/4$ [28,29]. The study of domain wall dynamics in the creep regime is crucial as it can reveal key magnetic properties under easily accessible experimental conditions. One particularly important property that can be extracted from the DW velocity is the DMI strength. This, among other methods, can be achieved by utilizing the symmetry-breaking effects of an additional in-plane (IP) magnetic field, which, in the presence of DMI, induces a measurable distortion of the magnetic bubble [16]. This asymmetric expansion along the profile of the bubble originates from the modification of the domain wall energy density caused by the interplay between the DMI and the applied IP field [11,17]. Assuming a magnetic bubble domain in the presence of perpendicular magnetic anisotropy (PMA), interfacial Dzyaloshinskii-Moriya interaction, and applied IP field along the bubble profile [see Fig. 1(a)], the DW surface energy density $\bar{\sigma}_{\mathrm{DW}}$ ($[\bar{\sigma}_{\mathrm{DW}}] = \mathrm{J/m^2}$) is given by [17]

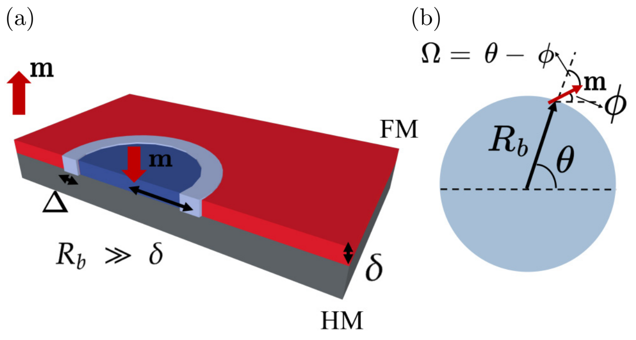

FIG. 1. (a) Bubble domain in a typical bilayer structure [heavy metal (HM)/ferromagnet (FM)] with Dzyaloshinskii-Moriya interaction and perpendicular magnetic anisotropy. Δ represents the domain wall (DW) width, R_b represents the bubble radius, and $\delta \ll R_b$ represents the sample thickness. The red and blue regions represent areas of opposite magnetization. (b) Magnetic bubble parameters: θ represents the angle that parameterizes the location of the bubble edge and ϕ represents the in-plane magnetization angle in the middle of the DW, i.e., where we do not have a vertical component m_z.

$$\bar{\sigma}_{\mathrm{DW}}(H_x, \theta, \phi) = 4\sqrt{AK_{\mathrm{eff}}} - \pi M_s \Delta \mu_0 (H_D \cos(\theta - \phi) + H_x \cos(\phi)) + \frac{\ln(2)}{\pi} \delta \mu_0 M_s^2 \cos^2(\theta - \phi), \tag{1}$$

where A represents exchange stiffness, K_{eff} is the effective anisotropy, M_s is the saturation magnetization, $\Delta = \sqrt{A/K_{\mathrm{eff}}}$ is the DW width, H_D is the DMI effective field, δ is the sample thickness, and $\{\phi, \theta\}$ represent, respectively, the domain wall magnetization angle and the angular coordinate along the circumference of the bubble [see Fig. 1(b)]. We identify the angle θ dependent equilibrium energy density of the magnetic bubble as

$$\bar{\mathcal{E}}_{\mathrm{DW}}(H_x, \theta) = \min_{\phi \in [0, 2\pi)} \bar{\sigma}_{\mathrm{DW}}(H_x, \theta, \phi). \tag{2}$$

This equilibrium domain wall energy density translates to the angle-dependent velocity $v(\theta)$ of the bubble as follows [17]:

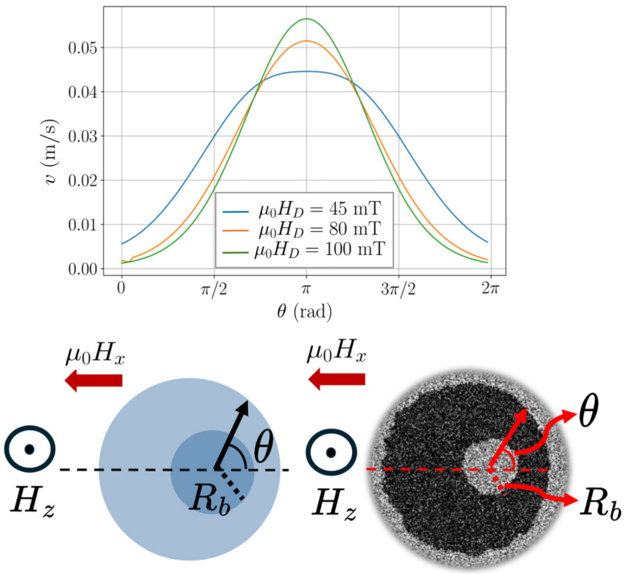

FIG. 2. (Top) Domain wall velocity as a function of the angle θ [see Eq. (1)] for three different values of the Dzyaloshinskii-Moriya interaction (DMI) field with a constant applied in-plane (IP) field $\mu_0 H_x = -80$ mT. The parameters used are $M_s = 1.2$ MA/m, $K_{\text{eff}} = 0.513$ MJ/m^3, $\alpha_0 = 15.47$ T$^{1/4}$, $\ln v_0 = 40.5$, and the out-of-plane (OOP) field is given by $\mu_0 H_z = 13.4$ mT. (Bottom) Representative illustration (left) of the experimentally measured asymmetric bubble expansion (right) in the presence of DMI, IP applied field $\mu_0 H_x$, and an OOP field $\mu_0 H_z$. R_b represents the radius of the initially nucleated bubble.

$$v(\theta, H_z) = v_0 \exp\left(-\alpha_0 \left(\frac{\bar{\mathcal{E}}_{\text{DW}}(H_x, \theta)}{\bar{\mathcal{E}}_{\text{DW}}(0, \theta)\mu_0 H_z}\right)^{1/4}\right), \tag{3}$$

where v_0 and α_0 are experimentally measured creep parameters (see Sec. IV). $v(\theta)$ can then be used to fit the experimentally determined angle-dependent velocity of the DW and extract important physical parameters of the sample such as the DMI strength [17] (see Fig. 2).

A. Extended creep model

Up to this point, we have completely omitted any radius dependence in the energy density, effectively treating the domain wall velocity with a true one-dimensional model [16]. If instead we introduce a domain wall energy density that takes into account the bubble curvature [30,31] (see Appendix A for a brief reminder of the derivation), the energy density of Eq. (1) becomes

$$\sigma_{\text{DW}}(H_x, \theta, \phi, R_b) = \Big[4\sqrt{AK_{\text{eff}}} - \pi M_s \Delta \mu_0 (H_D \cos(\theta - \phi) + H_x \cos(\phi)) + \frac{\ln(2)}{\pi}\delta \mu_0 M_s^2 \cos^2(\theta - \phi)\Big] + \frac{2A\Delta}{R_b^2} \tag{4}$$

$$= \bar{\sigma}_{\text{DW}} + \frac{2A\Delta}{R_b^2}, \tag{5}$$

where we have defined $\bar{\sigma}_{\text{DW}}$ as the radius-independent part of the energy density, equivalent to Eq. (1). The corresponding equilibrium energy density of the DW at each angle θ is

$$\mathcal{E}_{\text{DW}}(\theta, H_x, R_b) = \min_{\phi \in [0, 2\pi)} \sigma_{\text{DW}}(H_x, \theta, \phi, R_b) = \bar{\mathcal{E}}_{\text{DW}} + \frac{2A\Delta}{R_b^2}. \tag{6}$$

We can now write the equations of motion of a DW parameterized by the collective coordinates $\{R_b(t), \Omega(t)\}$ by expressing the Lagrangian density $\mathcal{L}$ and the Rayleigh dissipation function $\mathcal{F}$ as follows [32,33]:

$$\mathcal{L} = \sigma_{\text{DW}} + \frac{\mu_0 M_s}{\gamma_0} 2\pi \dot{\Omega} R_b^2, \tag{7}$$

$$\mathcal{F} = \frac{2\pi\alpha\mu_0 M_s R_b}{\gamma_0}\left(\frac{\dot{R}_b^2}{\Delta} + \Delta\dot{\Omega}^2\right), \tag{8}$$

where $\Omega = \theta - \phi$ represents the magnetization angle along the border of the bubble and R_b represents the bubble radius [see Fig. 1(a)]. Since we are primarily interested in the dynamics of the DW coordinate $R_b(t)$ (i.e., the velocity of the DW), we neglect the dynamics of the magnetization angle $\Omega(t)$ and only derive the DW velocity $\dot{R}_b$ using the Euler-Lagrange-Rayleigh equation,

$$\dot{R}_b \propto \alpha \left[H_z - \frac{1}{2\mu_0 M_s R_b}\left(\bar{\sigma}_{\text{DW}} - \frac{2A\Delta}{R_b^2}\right)\right] + \frac{1}{2}\left(\pi H_D \sin\Omega - \frac{\ln(2)}{2\pi\Delta}\delta M_s \sin(2\Omega)\right). \tag{9}$$

Neglecting higher orders in $1/R_b$, we can rewrite the equation of the DW velocity as

$$\dot{R}_b \propto \alpha \left[H_z - \frac{\bar{\sigma}_{\text{DW}}}{2\mu_0 M_s R_b}\right] + \frac{1}{2}\left(\pi H_D \sin\Omega - \frac{\ln(2)}{2\pi\Delta}\delta M_s \sin(2\Omega)\right) + \mathrm{O}\left(\frac{1}{R_b^2}\right). \tag{10}$$

At this point we can observe how the term $\bar{\sigma}_{\text{DW}}/2\mu_0 M_s R_b$ can be interpreted as a Laplace pressure term [20,21] competing with the external field H_z (see Fig. 3). In the following, we show what effects this additional term might have on the velocity of the DW in the creep regime, and the relative consequences for the determination of physical quantities related to it. First, let us consider a straight DW that is deformed through the application of an external force such as an applied magnetic field H_z perpendicular to the plane of the sample. We shall assume that the lateral deformation is of size L and the longitudinal displacement

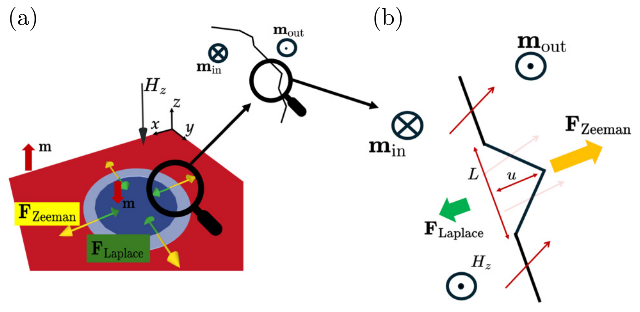

FIG. 3. (a) Macroscopic picture of the force balance at the boundary of a magnetic bubble in the presence of an applied magnetic field H_z and a competing Laplace pressure generated by the surface tension of the bubble. The inset depicts a more realistic picture of an actual boundary between domains [15,23] (observe the irregular pattern). (b) Microscopic picture of the domain wall (DW) segment deformation in response to the application of a driving force ($\mathbf{F}_{\rm Zeeman}$) and a competing Laplace force ($\mathbf{F}_{\rm Laplace}$). L and u represent the geometrical parameters of the DW deformation.

of the wall is identified by u (see Fig. 3). The energy balance $\Delta E_{\rm balance}(u,L)$ determining the dynamics of the DW in the creep regime is expressed by the competition between:

(1) Zeeman energy gain

$$-\mu_0 M_s H_z \frac{\delta L u}{2},$$

(2) elastic energy cost

$$2\frac{u^2}{\delta L}\mathcal{E}_{\rm DW},$$

(3) pinning energy gain

$$-\sqrt{\gamma\xi^2 L},$$

where γ has units $[\gamma] = J^2/m^3$ and represents the typical pinning potential strength, while ξ has units $[\xi] = m$ and represents the correlation length of the pinning centers [15,23,24].

If we now consider the finite radius of the bubble, according to Eq. (10), there is an additional term acting on the energy balance in a fashion similar to the hydrostatic pressure (or Laplace pressure) acting on the surface of a soap bubble [19–21],

$$\frac{\bar{\mathcal{E}}_{\rm DW}\delta L u}{2R_b}, \tag{11}$$

where R_b represents the radius of the magnetic bubble. As can be seen from this expression, the Laplace pressure term competes with the driving force $\propto H_z$ and can therefore be included in the energy balance as

$$\Delta E_{\rm balance}(u,L) = \mathcal{E}_{\rm DW}\frac{2u^2}{\delta L} - \sqrt{\gamma\xi^2 L} + \left(\frac{\bar{\mathcal{E}}_{\rm DW}}{R_b} - M_s H_z \mu_0\right)\frac{\delta L u}{2}, \tag{12}$$

which can easily be recast in the form [15]

$$\Delta E_{\rm balance}(u,L) = \mathcal{E}_{\rm DW}\frac{2u^2}{\delta L} - \sqrt{\gamma\xi^2 L} - \mu_0 M_s \tilde{H}_z(R_b)\frac{\delta L u}{2} \tag{13}$$

by modifying the applied field H_z by an R_b-dependent effective field $\tilde{H}_z(R_b)$,

$$\tilde{H}_z(R_b) = \left(H_z - \frac{\bar{\mathcal{E}}_{\rm DW}}{\mu_0 M_s R_b}\right). \tag{14}$$

The advantage of this approach is that it allows us to generalize the creep theory immediately by modifying the force term $H_z^{-1/4} \to \tilde{H}_z(R_b)^{-1/4}$ in the expression of the velocity in the creep regime of Eq. (3). The DW velocity as a

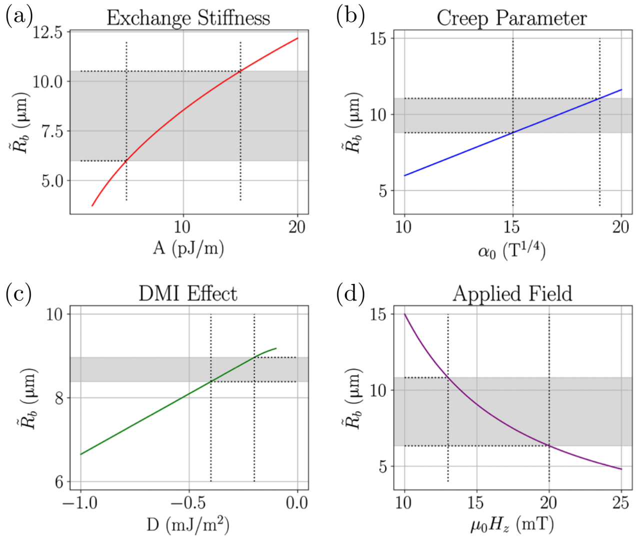

FIG. 4. Effect of different physical parameters on $\tilde{R}_b$ of Eq. (18). (a) Effect of exchange stiffness A, (b) effect of the creep parameter α_0, (c) effect of Dzyaloshinskii-Moriya interaction (DMI) strength D, (d) effect of applied field $\mu_0 H_z$. The applied out-of-plane field in all cases except in (d) is $\mu_0 H_z = 15$ mT. The areas highlighted in gray are a guide to the estimated strength of the effect and refer to the regions of interest (reported on the x axis of the plots) for the experimental parameters of the present samples [12]. The nonchanging parameters used in the respective plots are $A = 11.2$ pJ/m, $M_s = 1.2$ MA/m, $K_{\rm eff} = 0.513$ MJ/m^3, $\alpha_0 = 15.47$ T$^{1/4}$, $\mu_0 H_D = -30$ mT.

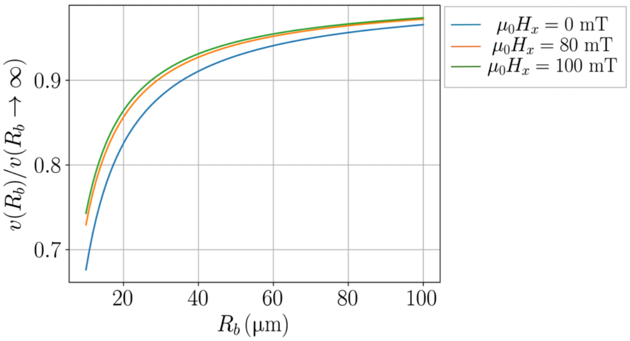

FIG. 5. Normalized velocity $v(R_b)/v(R_b \to \infty)$ as a function of the initial bubble radius R_b in the presence of an additional in-plane field $\mu_0 H_x$ as predicted by Eq. (16). The parameters used are $M_s = 1.2$ MA/m, $K_{\text{eff}} = 0.513$ MJ/m^3, $\alpha_0 = 15.47$ T$^{1/4}$, $\ln v_0 = 40.5$, $\mu_0 H_D = -20$ mT, $\mu_0 H_z = 15.45$ mT.

function of the initial radius R_b of the bubble domain can be expressed as

$$v(\theta, H_x, H_z, R_b) = v_0 \exp\left[-\alpha_0\left(\frac{(\bar{\mathcal{E}}_{\text{DW}}(\theta, H_x) + 2A\Delta/R_b^2)}{\tilde{H}_z(R_b)(\bar{\mathcal{E}}_{\text{DW}}(\theta, 0) + 2A\Delta/R_b^2)}\right)^{1/4}\right], \tag{15}$$

where we have used the fact $\mathcal{E}_{\text{DW}} = \bar{\mathcal{E}}_{\text{DW}} + 2A\Delta/R_b^2$ to make the radius dependence of the velocity explicit. To compare the velocity behavior across a variety of different samples, it is useful to normalize Eq. (15) with respect to the value of the velocity in the case of a straight DW, i.e., a magnetic bubble with an approximately infinite radius. In the absence of applied IP fields we can write

$$\frac{v(0,0,H_z,R_b)}{v(0,0,H_z,R_b \to \infty)} = \exp\left[-\alpha_0 \mu_0^{-1/4}(\tilde{H}_z(R_b)^{-1/4} - H_z^{-1/4})\right]. \tag{16}$$

To assess the effect of the different physical parameters on the strength of the radius-dependent effect, we can invert Eq. (16) and define $\tilde{R}_b$ as the radius value for which the DW velocity is halved, i.e.,

$$\frac{v(\tilde{R}_b)}{v(R_b \to \infty)} := \frac{1}{2} \tag{17}$$

$$\Rightarrow \tilde{R}_b = \frac{\bar{\mathcal{E}}_{\text{DW}}}{2\mu_0 M_s} \frac{1}{\left[H_z^{-1/4} + \frac{\mu_0^{1/4} \ln 2}{\alpha_0}\right]^4}. \tag{18}$$

$\tilde{R}_b$ can function as a metric for the strength of the pressure effect on the dynamics of the DW.

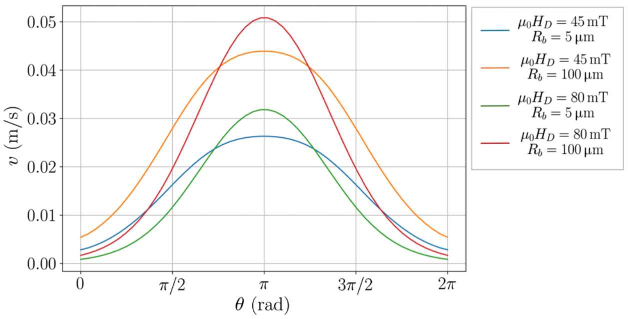

FIG. 6. Effect of the finite radius on the velocity profile of the bubble according to Eq. (15) for different values of the Dzyaloshinskii-Moriya interaction strength. The parameters used are $M_s = 1.2$ MA/m, $K_{\text{eff}} = 0.513$ MJ/m^3, $\alpha_0 = 15.47$ T$^{1/4}$, $\ln v_0 = 40.5$, while the out-of-plane field is $\mu_0 H_z = 13.4$ mT.

III. MODEL PREDICTIONS

As a first step to understanding the importance of the Laplace pressure term [see Eq. (16)] in samples with varying magnetic and disorder properties, we observe how the different physical parameters affect its strength, which we quantify through the $\tilde{R}_b$ parameter of Eq. (18). In Fig. 4 we show how exchange stiffness A [Fig. 4(a)], creep parameter α_0 [Fig. 4(b)], DMI strength D [Fig. 4(c)], and the applied field $\mu_0 H_z$ [Fig. 4(d)] can affect the parameter $\tilde{R}_b$ [see Eq. (18)]. The gray region in Fig. 4 indicates a typical range of physical parameters that might be observed in samples exhibiting bubble domains, such as the Pt/Co multilayers studied here. As we can see by comparing Figs. 4(c) and 4(a), the DMI strength has a smaller effect on the $\tilde{R}_b$ parameter when compared to the effect of the exchange stiffness A. We also emphasize how the creep parameter α_0, which, at fixed $\bar{\mathcal{E}}_{\text{DW}}$, depends on a combination of the disorder parameters introduced in Sec. II [15,23] (see Appendix C), has an effect on $\tilde{R}_b$, showing how the magnitude of this effect in the creep regime can also be influenced by the disorder characteristics of the material and not only by its magnetic properties.

The determination of the DMI strength from the experimental measurement of DW velocity in the creep regime requires the concurrent presence of an IP field H_x, as this is necessary to introduce the asymmetry in the bubble expansion [16,17]. The presence of this additional H_x field indeed alters the strength of the effect on the radius dependence (see Fig. 5) and induces a noticeable change on the velocity profile of the bubble. In Fig. 6 we can clearly see how the model predicts a marked change in the velocity

TABLE I. Co-based samples with Pt and Ir heavy metal layers.

Sample	Bottom layer (nm)	Ferromagnetic layer (nm)	Top layer (nm)
a_4	Ta(5)/Pt(3)	Co(0.8)	Ir(1)/Ta(3)
a_3	Ta(5)/Pt(3)	Co(0.8)	Ir(3)/Ta(3)

TABLE II. Experimentally obtained physical parameters of the a_4 and a_3 samples. M_s represents the saturation magnetization, K_{eff} represents the effective anisotropy, A represents the exchange stiffness. α_0 and $\ln v_0$ represent, respectively, the slope and the intercept of the creep data (see IV A and Fig. 7).

Sample	M_s (MA/m)	K_{eff} (MJ/m^3)	A (pJ/m)	α_0 (T$^{1/4}$)	$\ln v_0$
a_4	1.20 ± 0.09	0.513 ± 0.002	11 ± 2	15.5 ± 0.4	40 ± 1
a_3	1.14 ± 0.05	0.414 ± 0.001	10	20 ± 1	49 ± 3

profile of the DW along the circumference of the bubble with different $\mu_0 H_D$ and initial radius R_b combinations. Therefore, the radius dependence cannot be neglected in models aiming at describing bubble DW motion in a more general sense (i.e., across different bubble sizes).

IV. EXPERIMENTAL METHODS

A. Materials and methods

As discussed in Secs. II and II A, the presence of the additional Laplace pressure term [see Eq. (16)] can lead to a significant change in the velocity of the DW when the radius of the bubble domain is small enough. To validate this theoretical prediction and its implications, we have conducted a series of DW velocity measurements in both the presence and absence of IP fields at fixed H_z while varying the initial radius R_b of the bubble domain. We investigated two common magnetic Pt/Co multilayer compositions that are known to display sizable DMI [12]. Sample a_4 has a composition of Ta(5 nm)/Pt(3 nm)/Co(0.8 nm)/Ir(1 nm)/Ta(3 nm), while sample a_3 has composition Ta(5 nm)/Pt(3 nm)/Co(0.8 nm)/Ir(3 nm)/Ta(3 nm) (see Table I).

The saturation magnetization M_s was measured using a superconducting quantum interference device vibrating sample magnetometer (SQUID-VSM). The effective

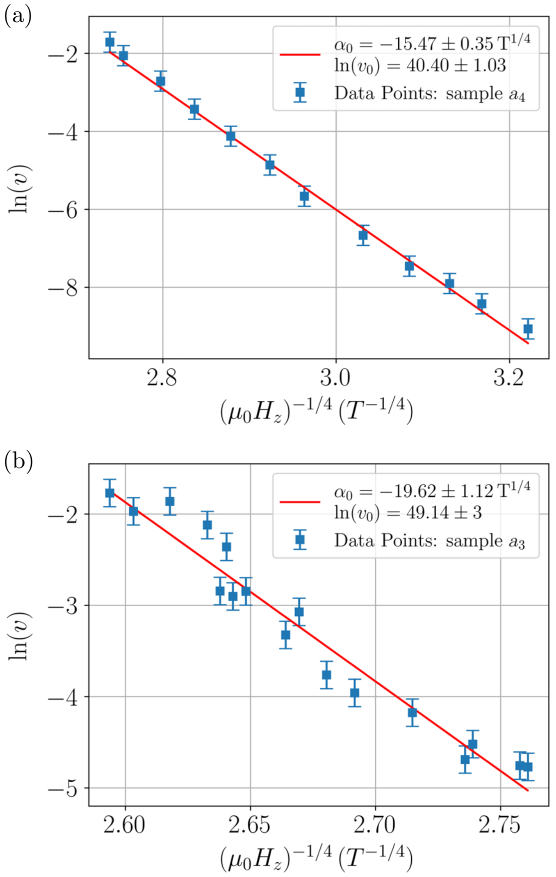

FIG. 7. Linear fit of Eq. (20) on the experimentally measured values of the domain wall velocity v as a function of the applied out-of-plane field $\mu_0 H_z$ [see Eq. (20)]. The top figure (a) refers to the creep measurement performed on sample a_4 and the bottom figure (b) represents the creep measurement performed on sample a_3 (see Table II). The values in the legend correspond to the creep parameters.

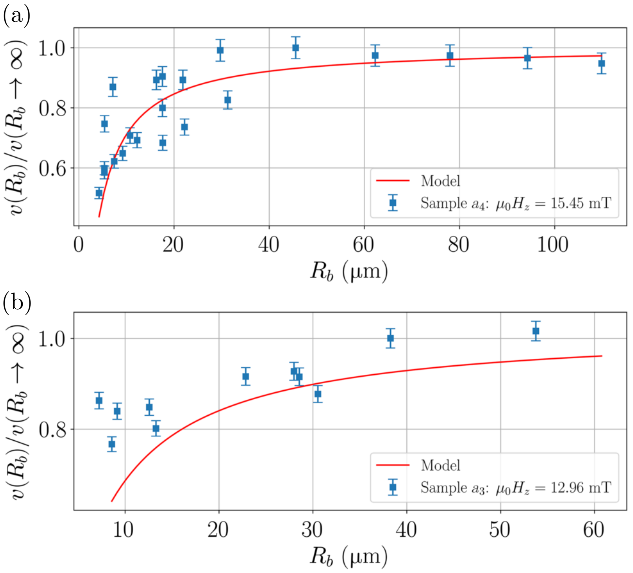

FIG. 8. (a) Radius dependence of the domain wall (DW) velocity in the a_4 sample (see Table II). The red curve represents a best fit of exchange stiffness A performed on the function of Eq. (16). The parameters used are $M_s = 1.2$ MA/m, $K_{\mathrm{eff}} = 0.513$ MJ/m^3, $\alpha_0 = 15.47$ T$^{1/4}$, $\ln v_0 = 40.5$. (b) Radius dependence of the DW velocity in the a_3 sample (see Table II). The red curve represents a suitable choice of exchange stiffness A performed on the function of Eq. (16). In this case a numerical failure prevented a true fitting procedure, and thus, an error estimation. The parameters used are $M_s = 1.14$ MA/m, $K_{\mathrm{eff}} = 0.414$ MJ/m^3, $\alpha_0 = 19.62$ T$^{1/4}$, $\ln v_0 = 50.29$ For both curves, a value of $\mu_0 H_D = -20$ mT is used.

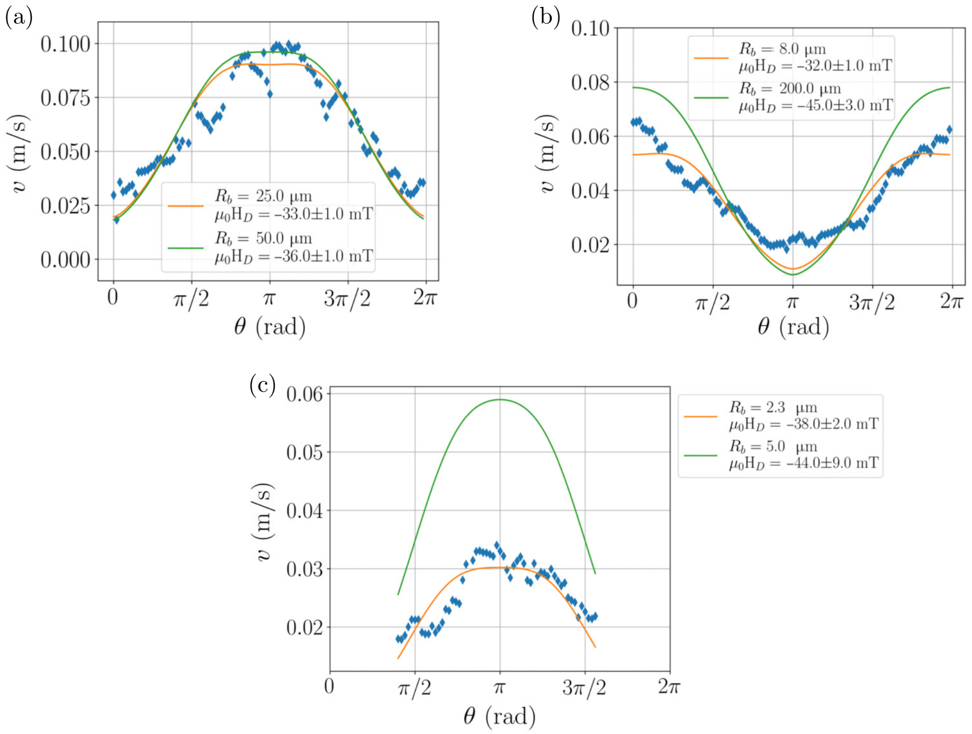

FIG. 9. Sample a_4: Domain wall velocity as a function of the θ angle (see Fig. 1). We show the comparison of the fit between using the experimentally measured R_b (orange curve) and a larger value of R_b (green curve). The three plots represent measurements and fits performed on bubble domains of initial radius $R_b \approx 25$ μm and in-plane (IP) field $\mu_0 H_x = 80$ mT (a), $R_b \approx 8$ μm and IP field $\mu_0 H_x = -102$ mT (b), $R_b \approx 2.3$ μm and IP field $\mu_0 H_x = 110$ mT (c). The parameters used are $M_s = 1.2$ MA/m, $K_{\text{eff}} = 0.513$ MJ/m^3, $\alpha_0 = 15.47$ T$^{1/4}$, $\ln v_0 = 40.5$, $\mu_0 H_z = 13.4$ mT.

anisotropy K_{eff} in the thin-film limit can be approximated by [34]

$$K_{\text{eff}} = K_u - \frac{1}{2}\mu_0 M_s^2, \tag{19}$$

where K_u represents uniaxial magnetocrystalline anisotropy and $-1/2\mu_0 M_s^2$ represents the demagnetization energy density contribution and is obtained by measuring magneto-optical Kerr rotation loops as a function of an in-plane magnetic field. The results were then fitted by minimizing the energy density $E = K_{\text{eff}} \sin^2\theta + K_{\text{eff}} \sin^4\theta - H_{\text{ext}} M_s \cos(\theta - \phi)$, where θ is the angle between the applied field H_{ext} and M_s, and ϕ is the angle between H and the easy axis [3].

The exchange stiffness was extrapolated by measuring the velocity as a function of initial bubble radius, following model predictions (see Secs. III and IV B for the details). The error could not always be estimated, as fitting on sample a_3 resulted in numerical failure, requiring a manual selection of A. All measured values are reported in Table II. The extraction of the creep parameters α_0, v_0 necessary for the correct estimation of the DW velocity in the model of Eq. (16) was performed on the velocity curve of the DW as a function of the applied field H_z in the creep regime. Equation (3) in the absence of IP fields (i.e., $\mu_0 H_x = 0$) can be expressed as [23]

$$\ln v = \ln v_0 - \alpha_0 (\mu_0 H_z)^{-1/4}, \tag{20}$$

which can then be used as a linear fit on the experimental data to extract α_0 (corresponding to the slope) and v_0 (corresponding to the intercept), as can be seen in Fig. 7. To obtain an independent estimate of the value of the DMI coupling constant D, samples a_3 and a_4 was also studied by BLS. As a matter of fact, by measuring the Stokes–anti-Stokes peak asymmetry it is possible to extract a value of D, as explained in detail in Ref. [12]. BLS measurements were repeated in several different areas of the sample surface in order to obtain an average value that could be representative of the whole sample. The resulting value is $D_{\text{BLS}}(a_4) = -0.8 \pm 0.1$ mJ/m^2.

B. Results and discussion

Figure 8 shows the normalized DW velocity as a function of the initial bubble radius R_b. Both samples a_4 and a_3 display a decrease of the DW velocity below certain values of R_b. We furthermore notice how the experimentally measured trends are followed by the theoretical prediction expressed with the velocity formula of Eq. (16) (observe the continuous curves in Fig. 8). We fit Eq. (10) and extract the exchange stiffness A from the data reported in Fig. 8. For both curves in Fig. 8, a value of $\mu_0 H_D = -20$ mT was used. This is reasonable since the DMI has a small influence on $\tilde{R}_b$ with respect to the exchange stiffness in these samples [see Fig. 4(c)]. The obtained values for A are reported in Table II and are used in the following. We highlight the fact that the obtained exchange stiffness values are higher than those obtained in Ref. [12] for the same samples but are closer to literature values reported for similar samples [15]. We notice how the range of accessible initial bubble radii R_b is larger in sample a_4 as compared to sample a_3: this is due to the higher nucleation density of bubble domains in sample a_3 causing a narrower window of bubble radii in which domain expansion can occur without colliding with neighboring ones. The radius dependence of the DW of velocity displayed in Fig. 8 shows how additional care might be required in the determination of physical quantities measured via DW expansion in the creep regime.

The DW Laplace pressure may have a strong influence on the experimental determination of DW speed from bubble expansion experiments in the creep regime. This leads to implications for measurement purposes, as is the case for the DMI strength measured via the protocol proposed by Ref. [17] (see Appendix C). We therefore performed domain expansion experiments under the application of IP fields on a variety of bubble sizes. In particular, we measured asymmetric bubble expansion with an IP field for bubbles with an initial radius of $R_b \approx 2.3$, 8, and 25 μm in sample a_4 (see Fig. 9) and $R_b \approx 8$ and 77 μm in sample a_3 (see Fig. 10). After the experimental determination of $v(\theta)$ (see Fig. 2) for the different bubbles, we proceeded to fit $v(\theta, R_b)$ from Eq. (16) on the measured data in the samples a_4 and a_3. To highlight the initial radius R_b dependence, we use the following scheme: in one case we use a larger R_b value in the $v(\theta, R_b)$ from Eq. (16) to show the effect of neglecting the correct bubble radius (see the green curves in Figs. 9 and 10), while in the other case we use the experimentally measured bubble radius R_b (see the orange curves in Figs. 9 and 10). Focusing on sample a_4, we can observe [Fig. 9(a)] how, in the case of large bubbles ($R_b \approx 25$ μm), considering the correct radius has a small effect on the success of the fit: fitting the curve with either $R_b = 25$ μm or $R_b = 60$ μm causes the value of $\mu_0 H_D$ to change by 2 mT. On the other hand, in the regime where the Laplace pressure becomes sizable (see Fig. 6), the experimentally determined DW velocity becomes highly sensitive to even small variations in R_b. The sizable effect of the Laplace pressure needs to be taken in consideration here, as the fits of Figs. 9(b) and 9(c) (observe the green curves) evidence how the incorrect assumption of the bubble radius R_b results in the failure of the fitting procedure. Using the correct values of R_b, on the other hand [see the orange curves of Figs. 9(b) and 9(c)], shows the success of the fit and how the consistency of the $\mu_0 H_D$ is preserved across different bubble dimensions. An analogy can be found using the same procedure on sample a_3, where, in Fig. 10(a), the relatively large initial radius of the bubble (77 μm) causes the error to be small compared to Fig. 10(b), where taking into account the correct value of the initial radius ($R_b \approx 8$ μm) has a visible impact on the success of the fit. As a final remark, we emphasize how the obtained values of the DMI effective field [$\mu_0 H_D(a_3) \approx -22.1 \pm 0.6$ mT and $\mu_0 H_D(a_4) \approx -33 \pm 4$ mT] are in agreement with the values reported in Ref. [12]. The higher values of the DMI energy obtained through $D = \mu_0 H_D M_s \Delta$ [$D(a_3) = -0.124 \pm 0.006$ mJ/m^2, $D(a_4) = -0.18 \pm 0.03$ mJ/m^2] are related to the higher values of exchange stiffness A. We also note that the higher D values are closer to (yet still smaller than) DMI energy strength values obtained through independent BLS measurements [$D_{\mathrm{BLS}}(a_4) = -0.8 \pm 0.1$ mJ/m^2 and $D_{\mathrm{BLS}}(a_3) = -0.5 \pm 0.1$ mJ/m^2 [13]]. The discrepancy between DMI values reported via DW speed measurements in the creep regime and BLS measurements is a well-known issue [13] that will be addressed in future work. The modified creep model of Eq. (16), which accounts for the additional Laplace pressure felt by magnetic bubble domains, eliminates the

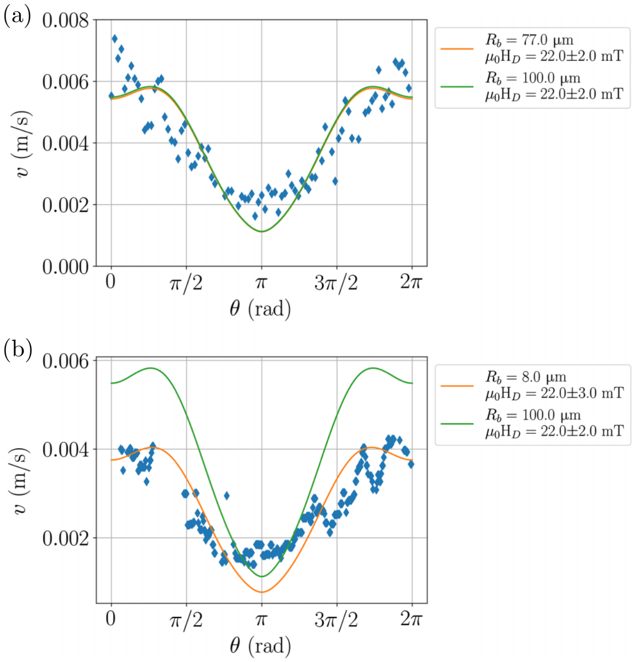

FIG. 10. Sample a_3: Domain wall velocity as a function of the θ angle (see Fig. 1). We show the comparison of the fit between using the experimentally measured R_b (orange curve) and a larger value of R_b (green curve). The two plots represent measurements and fits performed on bubble domains of initial radius $R_b \approx 77$ μm (a), $R_b \approx 8$ μm (b). Both the measurements were performed with an in-plane field of $\mu_0 H_x = -80$ mT. The parameters used are $M_s = 1.14$ MA/m, $K_{\mathrm{eff}} = 0.414$ MJ/m^3, $\alpha_0 = 19.62$ T$^{1/4}$, $\ln v_0 = 50.29$, $\mu_0 H_z = 12.96$ mT.

inconsistency of the DMI values obtained by fitting the $v(\theta)$ curves with the $R_b \to \infty$ model [i.e., that of Eq. (3)]. This not only improves the measurement reproducibility, but can also prove necessary in cases where the actual space to allow for a complete expansion of a bubble domain under an IP field without impinging on sample barriers or other bubbles is lacking. In particular, the method discussed in Ref. [17] enhanced by the radius dependence of the velocity of Eq. (16) could allow for the *in situ* measurements of DMI on patterned samples for device applications in which the surface area of magnetic material might be severely reduced compared with fully homogeneous films.

V. CONCLUSIONS

In this paper, we demonstrate how the DW velocity of magnetic bubble domains in the creep regime displays a significant reduction below a sample-dependent threshold radius [19] in thin-film Pt(3 nm)/Co(0.8 nm)/Ir(1 nm) and Pt(3 nm)/Co(0.8 nm)/Ir(3 nm) samples. We show that this phenomenon is due to the Laplace pressure felt by the magnetic bubble and provide an extension of the creep model for DW motion that is able to describe this dependence. To have a consistent description of the phenomenon, we have to include a radius-dependent term both in the energy density of the DW, and in the driving force term of the creep law [see Eq. (15)]. To highlight the possible consequences of neglecting this term in models describing DW motion in the creep regime, we study the case of the determination of the DMI strength from asymmetric bubble expansion [16,17]. We show how accounting for the Laplace pressure term is necessary for obtaining reproducible DMI measurements when dealing with bubbles of varying size (Figs. 9 and 10). We also stress the fact that the radius dependence becomes increasingly relevant when the creep regime is only accessible with low OOP fields. Therefore, we conclude that a reproducible measurement of magnetic properties related to creep DW velocity in magnetic bubbles requires an initial assessment and study of the radius dependence of the DW velocity. The technique introduced in Ref. [17], when coupled with the radius-dependent correction of Eq. (16), can be used to measure the DMI on reduced portions of magnetic materials such as patterned surfaces, as might be the case for *in situ* measurements of finished devices.

ACKNOWLEDGMENTS

We thank Stefania Pizzini and Laurent Ranno (Institut Néel, Grenoble) for useful and inspiring discussions. This project is supported by the European Union (EU) and the Italian ministry of University and Research (MUR) under the grant PRIN 2022 “Metrology for spintronics: A machine learning approach for the reliable determination of the Dzyaloshinskii-Moriya interaction (MetroSpin)” Codice di progetto: 2022SAYARY, CUP E53D23001830006 PIANO NAZIONALE DI RIPRESA E RESILIENZA (PNRR) Missione 4 “Istruzione e Ricerca” - Componente C2 Investimento 1.1, “Fondo per il Programma Nazionale di Ricerca e Progetti di Rilevante Interesse Nazionale (PRIN)” Decreto Direttoriale n. 104 del 2 febbraio 2022.

DATA AVAILABILITY

The data that support the findings of this article are openly available [35], embargo periods may apply.

APPENDIX A: DERIVATION OF DOMAIN WALL ENERGY DENSITY FOR A BUBBLE DOMAIN

In the following we provide a brief reminder of how to derive the domain wall energy density for a curved domain as opposed to the usual derivation for linear domains [33]. The starting point is the energy density of a magnetized body of volume V with PMA,

$$E = \int_V \Bigg\{ \underbrace{A|\nabla \mathbf{m}|^2}_{\mathcal{E}_{\mathrm{exch}}} - \underbrace{D[m_z(\nabla\cdot\mathbf{m}) - (\nabla\cdot\mathbf{m})m_z]}_{\mathcal{E}_{\mathrm{DMI}}} - \underbrace{\frac{1}{2}\mu_0 M_s \mathbf{m}\cdot\mathbf{H}_d + K_u(\mathbf{m}\cdot\hat{\mathbf{u}}_{\mathbf{z}})^2}_{\mathcal{E}_{\mathrm{anis}}} - \underbrace{\mu_0 M_s \mathbf{m}\cdot\mathbf{H}}_{\mathcal{E}_{\mathrm{Zeeman}}} \Bigg\} d^3\mathbf{r}, \tag{A1}$$

where $\mathbf{m}(\mathbf{r},t) = \mathbf{M}(\mathbf{r},t)/M_s$ is the normalized magnetization vector, A represents the exchange stiffness, D represents the DMI constant, $\mathbf{H}_d$ is the magnetostatic field, and $\mathbf{H}$ is the applied field. If we express the normalized magnetization vector in spherical coordinates $\mathbf{m}(\mathbf{r},t) = (\sin\tilde{\theta}\cos\phi, \sin\tilde{\theta}\sin\phi, \cos\tilde{\theta})^T$ [where the angles $\tilde{\theta}(\mathbf{r},t), \phi(\mathbf{r},t)$ manifestly depend on the position $\mathbf{r}$ and the time instant t], we can write the different energy terms as

$$\mathcal{E}_{\mathrm{exch}} = A[(\nabla\tilde{\theta})^2 + \sin^2\tilde{\theta}(\nabla\phi)^2], \tag{A2}$$

$$\mathcal{E}_{\mathrm{DMI}} = D\left[\cos\phi\frac{\partial\tilde{\theta}}{\partial x} + \sin\phi\frac{\partial\tilde{\theta}}{\partial y} + \sin\tilde{\theta}\cos\tilde{\theta}\left(\sin\phi\frac{\partial\phi}{\partial x} - \cos\phi\frac{\partial\phi}{\partial y}\right)\right], \tag{A3}$$

$$\mathcal{E}_{\mathrm{anis}} = K_0\sin^2\tilde{\theta} + K\sin^2\tilde{\theta}\sin^2\phi, \tag{A4}$$

$$\mathcal{E}_{\mathrm{Zeeman}} = \mu_0 M_s(H_x\sin\tilde{\theta}\cos\phi + H_z\cos\tilde{\theta}). \tag{A5}$$

We have written the $\mathcal{E}_{\mathrm{anis}}$ term in a compact fashion as is usually done in the literature [33]: K_0 represents the effective anisotropy while K is the shape anisotropy. Converting the integration to cylindrical coordinates

$$x \to r\cos\theta \tag{A6}$$

$$y \to r\sin\theta \tag{A7}$$

$$z \to z' \tag{A8}$$

and making use of the Bloch ansatz for the DW profile [33]

$$\begin{cases} \tan(\tilde{\theta}(r)/2) = \exp\left(\frac{r-R_b}{\Delta}\right) \\ \phi(\theta) = \theta + \Omega, \end{cases} \tag{A9}$$

we can rewrite the integral of Eq. (A1) as

$$\begin{aligned} E = \delta \int_0^{2\pi}\int_0^{R_t} \Bigg\{ & A\left[\left(\frac{\partial\tilde{\theta}}{\partial r}\right)^2 + \frac{\sin^2\tilde{\theta}}{r^2}\right] \\ & - D\left[\frac{\partial\tilde{\theta}}{\partial r} + \frac{\cos\tilde{\theta}\sin\tilde{\theta}}{r}\right]\cos\Omega + \left(K_0 + K\sin^2\Omega\right) \\ & \times \sin^2\tilde{\theta} - \mu_0 M_s H_z \cos\tilde{\theta}\Bigg\}\, r\, dr\, d\theta, \end{aligned} \tag{A10}$$

where δ represents the thickness of the sample. We emphasize the distinction between $\tilde{\theta}$, which represents the magnetization angle with respect to the global $\hat{z}$ axis, and θ, which represents the polar angle used to parameterize space (see Fig. 11) To obtain the above form, we have exploited the fact that the energy density is independent of the z coordinate, i.e., the energy density is assumed constant along the z direction. At this point, to derive the energy density of the DW, we have to integrate out the r variable. To do so, we first of all notice that, from the ansatz of Eq. (A9), we have $\partial\tilde{\theta}/\partial r = \sin\tilde{\theta}/\Delta = (1/\Delta)\mathrm{sech}\big((r-R_b)/\Delta\big)$. Making the substitution $\eta = ((r-R_b)/\Delta)$, we obtain

$$\begin{aligned} E = \delta \int_0^{2\pi}\int_{-R_b/\Delta}^{(R_t-R_b)/\Delta} \Bigg\{ & A\sin^2\tilde{\theta}\left[\frac{1}{\Delta^2} + \frac{1}{(\Delta\eta + R_b)^2}\right] \\ & - D\left[\frac{\sin\tilde{\theta}}{\Delta} + \frac{\cos\tilde{\theta}\sin\tilde{\theta}}{\Delta\eta + R_b}\right]\cos\Omega + \left(K_0 + K\sin^2\Omega\right)\sin^2\tilde{\theta} \\ & - \mu_0 M_s (H_z\cos\tilde{\theta} + H_x\sin\tilde{\theta}\cos\Omega)\Bigg\}(\Delta\eta + R_b)\, dr\, d\theta, \end{aligned} \tag{A11}$$

which, in the limit $R_b/\Delta \gg 1$ and $\lim_{R_t\to\infty}$, is asymptotically equivalent to

$$\begin{aligned} E \sim \delta\Delta \int_0^{2\pi}\int_{-\infty}^{\infty} \Bigg\{ & A\,\mathrm{sech}^2(\eta)\left[\frac{1}{\Delta^2} + \frac{1}{(\Delta\eta + R_b)^2}\right] \\ & - D\left[\frac{\mathrm{sech}(\eta)}{\Delta} + \frac{\sqrt{1-\mathrm{sech}^2(\eta)}\,\mathrm{sech}(\eta)}{\Delta\eta + R_b}\right]\cos\Omega \\ & + \left(K_0 + K\sin^2\Omega\right)\mathrm{sech}^2(\eta) \\ & - \mu_0 M_s (H_z\sqrt{1-\mathrm{sech}^2(\eta)} + H_x\mathrm{sech}(\eta)\cos\Omega\Bigg\} \\ & \times (\Delta\eta + R_b)\, d\eta\, d\theta. \end{aligned} \tag{A12}$$

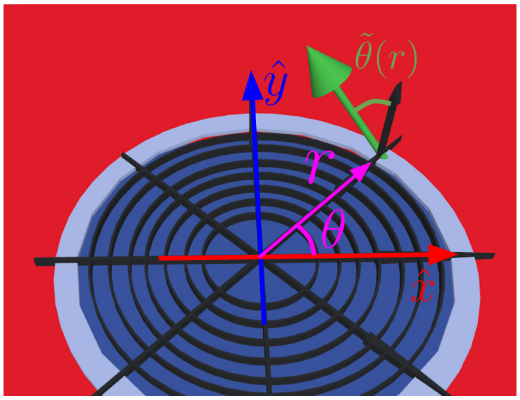

FIG. 11. Representation of the polar coordinates used to perform the integration of the energy density of Eq. (A10).

We can now use some known integration formulas for hyperbolic functions (see, e.g., Ref. [36]),

$$\int_{-\infty}^{\infty} \eta\,\mathrm{sech}^2(\eta) d\eta = 0, \tag{A13}$$

$$\int_{-\infty}^{\infty} \mathrm{sech}^2(\eta) d\eta = 2, \tag{A14}$$

$$\int_{-\infty}^{\infty} \mathrm{sech}(\eta) d\eta = \pi, \tag{A15}$$

$$\int_{-\infty}^{\infty} \sqrt{1-\mathrm{sech}^2(\eta)}\,\mathrm{sech}(\eta) d\eta = 2, \tag{A16}$$

as well as the fact that integrals of the form

$$\int_{-\infty}^{\infty} \frac{\mathrm{sech}^2(\eta)}{\Delta\eta + R_b} d\eta, \tag{A17}$$

only converge in the limit $R_b/\Delta \gg 1$, to obtain

$$\int_{-\infty}^{\infty} \frac{\mathrm{sech}^2(\eta)}{\Delta\eta + R_b} d\eta \approx \frac{2\Delta}{R_b}. \tag{A18}$$

Combining the above mentioned identities with Eq. (A12), we finally obtain the surface energy density of the bubble

$\sigma_{\rm DW}$ as a function of the bubble radius R_b and the angle Ω (see Fig. 1),

$$\frac{E}{2\pi t R_b} := \sigma_{\rm DW} = \left(4\sqrt{AK_{\rm eff}} - \pi D\cos\Omega + 2\Delta K\sin^2\Omega\right) + \frac{2A\Delta}{R_b^2} - 2\pi\mu_0 M_s H_z R_b. \tag{A19}$$

APPENDIX B: BRIEF REMINDER OF CREEP THEORY

In the following we provide a brief reminder of the origin of the creep relation reported in Eq. (20). For an in-depth review of the topic, we suggest Ref. [1] and references therein. As mentioned in Sec. II, the velocity of a domain wall in the creep regime is determined by the competition of thermal energy and energy barrier. The energy barrier encodes all the energy costs (elastic energy) and gains (Zeeman and pinning energy) the magnetic DW is subject to as a function of its dimension and configuration. The energy barrier is given by Eq. (13) in the main text. The velocity of the DW is determined by the ability of thermal fluctuations to overcome the highest possible value of the energy barrier, i.e., the extremal value of $\Delta E(u, L)$ [see Eq. (13)], where u and L are the geometrical parameters of the DW displacements displayed in Fig. 3(b). An important point, however, is that u and L are not independent of one another and are related by the exponential relation

$$u(L) = u_c\left(\frac{L}{L_c}\right)^{\zeta}, \tag{B1}$$

where u_c represents the transverse scaling parameter [37] and L_c represents the so-called Larkin length [38]. The Larkin length L_c is a characteristic length scale obtained by the optimal balance of the pinning energy and the elastic energy of Eq. (13) when the DW has jumped exactly one pinning center, i.e., $u = \xi$.

$$L_c = 2\left(2\frac{\bar{\mathcal{E}}_{\rm DW}\xi^2}{\gamma}\right)^{1/3}. \tag{B2}$$

On the other hand, ζ represents the critical exponent of this relation and is often referred to as the roughness exponent. Much like the creep critical exponent $\mu = 1/4$, $\zeta = 2/3$ depends on very fundamental properties of the theory, such as the dimensionality of the interface, etc. [39]. Equipped with $u(L)$, we can readily plug this expression into $\Delta E(u(L), L)$ and maximize it to obtain the energy barrier F_b.

$$F_b = \max_L \Delta E(u(L), L) = \frac{4}{5^{5/4}}\frac{u_c^{9/4}\sqrt{\gamma}}{\xi}\left(\frac{\bar{\mathcal{E}}_{\rm DW}}{H_z M_s}\right)^{1/4}, \tag{B3}$$

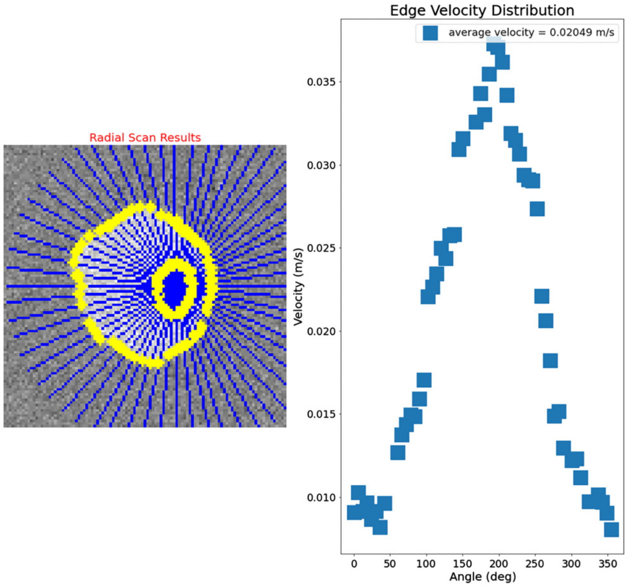

FIG. 12. Output of the bubble edge detection code based on the C2V PYTHON library [40].

which can then finally be plugged into the velocity to obtain the well-known creep law [23]

$$v = v_0 \exp(-\alpha_0 H_z^{-1/4}),$$

where the creep parameter α_0 is

$$\alpha_0 \propto \frac{4}{5^{5/4}}\frac{u_c^{9/4}\sqrt{\gamma}}{k_B T\xi}\left(\frac{\bar{\mathcal{E}}_{\rm DW}}{M_s}\right)^{1/4}. \tag{B4}$$

APPENDIX C: BUBBLE EXPANSION MEASUREMENT METHOD

The analysis of the bubble domain expansion is performed using polar Kerr magneto-optic principles, while the data analysis and the extraction of the velocities as a function of the angle $v(\theta)$ is performed using a custom written PYTHON-based user interface code. The user has to provide the center of the initial bubble manually and then the code proceeds to detect the edges using the PYTHON C2V library [40]. In Fig. 12, the left image represents the result of the edge detection analysis while the right image reports the measured velocities as a function of the θ angle (see Fig. 2 in the main text). The obtained velocity curves as a function of the θ angle are then used to perform the fits described in the main text (see Figs. 9 and 10).

[1] P. J. Metaxas, J. P. Jamet, A. Mougin, M. Cormier, J. Ferré, V. Baltz, B. Rodmacq, B. Dieny, and R. L. Stamps, Creep and flow regimes of magnetic domain-wall motion in ultrathin Pt/Co/Pt films with perpendicular anisotropy, Phys. Rev. Lett. **99**, 217208 (2007).

[2] F. Cayssol, D. Ravelosona, C. Chappert, J. Ferré, and J. P. Jamet, Domain wall creep in magnetic wires, Phys. Rev. Lett. **92**, 107202 (2004).

[3] L. Herrera Diez, F. García-Sánchez, J.-P. Adam, T. Devolder, S. Eimer, M. S. El Hadri, A. Lamperti, R. Mantovan, B. Ocker, and D. Ravelosona, Controlling magnetic domain wall motion in the creep regime in He^+-irradiated CoFeB/MgO films with perpendicular anisotropy, Appl. Phys. Lett. **107**, 032401 (2015).

[4] E. E. Ferrero, L. Foini, T. Giamarchi, A. B. Kolton, and A. Rosso, Creep motion of elastic interfaces driven in a disordered landscape, Annu. Rev. Condens. Matter Phys. **12**, 111 (2021).

[5] I. Dzyaloshinsky, A thermodynamic theory of “weak” ferromagnetism of antiferromagnetics, J. Phys. Chem. Solids **4**, 241 (1958).

[6] T. Moriya, Anisotropic superexchange interaction and weak ferromagnetism, Phys. Rev. **120**, 91 (1960).

[7] A. Fert, N. Reyren, and V. Cros, Magnetic skyrmions: advances in physics and potential applications, Nat. Rev. Mater. **2**, 1 (2017).

[8] A. Fert, V. Cros, and J. Sampaio, Skyrmions on the track, Nat. Nanotechnol. **8**, 152 (2013).

[9] G. Finocchio, F. Büttner, R. Tomasello, M. Carpentieri, and M. Kläui, Magnetic skyrmions: from fundamental to applications, J. Phys. D:Appl. Phys. **49**, 423001 (2016).

[10] A. Bogdanov, and A. Hubert, Thermodynamically stable magnetic vortex states in magnetic crystals, J. Magn. Magn. Mater. **138**, 255 (1994).

[11] A. Thiaville, S. Rohart, É. Jué, V. Cros, and A. Fert, Dynamics of Dzyaloshinskii domain walls in ultrathin magnetic films, Europhys. Lett. **100**, 57002 (2012).

[12] A. Magni *et al.*, Key points in the determination of the interfacial Dzyaloshinskii-Moriya interaction from asymmetric bubble domain expansion, IEEE Trans. Magn. **58**, 1 (2022).

[13] M. Küpferling, A. Casiraghi, G. Soares, G. Durin, F. García-Sánchez, L. Chen, C. Back, C. Marrows, S. Tacchi, and G. Carlotti, Measuring interfacial Dzyaloshinskii-Moriya interaction in ultrathin magnetic films, Rev. Mod. Phys. **95**, 015003 (2023).

[14] M. Vaňatka, J.-C. Rojas-Sánchez, J. Vogel, M. Bonfim, M. Belmeguenai, Y. Roussigné, A. Stashkevich, A. Thiaville, and S. Pizzini, Velocity asymmetry of Dzyaloshinskii domain walls in the creep and flow regimes, J. Phys.: Condens. Matter **27**, 326002 (2015).

[15] D. M. F. Hartmann, R. A. Duine, M. J. Meijer, H. J. M. Swagten, and R. Lavrijsen, Creep of chiral domain walls, Phys. Rev. B **100**, 094417 (2019).

[16] S.-G. Je, D.-H. Kim, S.-C. Yoo, B.-C. Min, K.-J. Lee, and S.-B. Choe, Asymmetric magnetic domain-wall motion by the Dzyaloshinskii-Moriya interaction, Phys. Rev. B **88**, 214401 (2013).

[17] T. Pakam, A. A. Adjanoh, S. D. M. Afenyiveh, J. Vogel, S. Pizzini, and L. Ranno, Anisotropic creep velocity of Dzyaloshinskii domain walls, Appl. Phys. Lett. **124**, 092403 (2024).

[18] J. P. Garcia, A. Fassatoui, M. Bonfim, J. Vogel, A. Thiaville, and S. Pizzini, Magnetic domain wall dynamics in the precessional regime: Influence of the Dzyaloshinskii-Moriya interaction, Phys. Rev. B **104**, 014405 (2021).

[19] K.-W. Moon, J.-C. Lee, S.-G. Je, K.-S. Lee, K.-H. Shin, and S.-B. Choe, Long-range domain wall tension in Pt/Co/Pt films with perpendicular magnetic anisotropy, Appl. Phys. Express **4**, 043004 (2011).

[20] Y. Zhang, X. Zhang, N. Vernier, Z. Zhang, G. Agnus, J.-R. Coudevylle, X. Lin, Y. Zhang, Y.-G. Zhang, W. Zhao, and D. Ravelosona, Domain-wall motion driven by Laplace pressure in Co-Fe-B/MgO nanodots with perpendicular anisotropy, Phys. Rev. Appl. **9**, 064027 (2018).

[21] X. Zhang, N. Vernier, W. Zhao, H. Yu, L. Vila, Y. Zhang, and D. Ravelosona, Direct observation of domain-wall surface tension by deflating or inflating a magnetic bubble, Phys. Rev. Appl. **9**, 024032 (2018).

[22] N. B. Caballero, E. E. Ferrero, A. B. Kolton, J. Curiale, V. Jeudy, and S. Bustingorry, Magnetic domain wall creep and depinning: A scalar field model approach, Phys. Rev. E **97**, 062122 (2018).

[23] S. Lemerle, J. Ferré, C. Chappert, V. Mathet, T. Giamarchi, and P. Le Doussal, Domain wall creep in an Ising ultrathin magnetic film, Phys. Rev. Lett. **80**, 849 (1998).

[24] P. Chauve, T. Giamarchi, and P. Le Doussal, Creep and depinning in disordered media, Phys. Rev. B **62**, 6241 (2000).

[25] T. A. Moore, I. Miron, G. Gaudin, G. Serret, S. Auffret, B. Rodmacq, A. Schuhl, S. Pizzini, J. Vogel, and M. Bonfim, High domain wall velocities induced by current in ultrathin Pt/Co/AlOx wires with perpendicular magnetic anisotropy, Appl. Phys. Lett. **93**, 262504 (2008).

[26] E. Jué, A. Thiaville, S. Pizzini, J. Miltat, J. Sampaio, L. Buda-Prejbeanu, S. Rohart, J. Vogel, M. Bonfim, O. Boulle *et al.*, Domain wall dynamics in ultrathin Pt/Co/AlOx microstrips under large combined magnetic fields, Phys. Rev. B **93**, 014403 (2016).

[27] G. Blatter, M. V. Feigel’man, V. B. Geshkenbein, A. I. Larkin, and V. M. Vinokur, Vortices in high-temperature superconductors, Rev. Mod. Phys. **66**, 1125 (1994).

[28] A.-L. Barabási, and H. E. Stanley, *Fractal Concepts in Surface Growth* (Cambridge University Press, Cambridge, United Kingdom, 1995).

[29] H. Ji, and M. O. Robbins, Transition from compact to self-similar growth in disordered systems: Fluid invasion and magnetic-domain growth, Phys. Rev. A **44**, 2538 (1991).

[30] J. Vandermeulen, S. Nasseri, B. Van de Wiele, G. Durin, B. Van Waeyenberge, and L. Dupré, Comparison between collective coordinate models for domain wall motion in PMA nanostrips in the presence of the Dzyaloshinskii-Moriya interaction, J. Magn. Magn. Mater. **449**, 337 (2018).

[31] S. Moretti, *Micromagnetic study of magnetic domain wall motion: thermal effects and spin torques*, Ph.D. thesis, Ediciones Universidad de Salamanca, 2017.

[32] M.-C. Ciornei, J. M. Rubí, and J.-E. Wegrowe, Magnetization dynamics in the inertial regime: Nutation predicted at short time scales, Phys. Rev. B **83**, 020410 (2011).

[33] *Spin Dynamics in Confined Magnetic Structures III* (Springer Berlin Heidelberg, Berlin, Germany, 2006).

[34] A. Aharoni, Demagnetizing factors for rectangular ferromagnetic prisms, J. Appl. Phys. **83**, 3432 (1998).

[35] https://zenodo.org/records/15805564.

[36] I. S. Gradštejn, J. M. Ryžik, A. Jeffrey, D. Zwillinger, and I. S. Gradštejn, *Table of Integrals, Series and Products* (Elsevier Acad. Press, Amsterdam, 2009), 7th ed.

[37] M. Kardar, and D. R. Nelson, Commensurate-incommensurate transitions with quenched random impurities, Phys. Rev. Lett. **55**, 1157 (1985).

[38] A. Larkin, and Y. N. Ovchinnikov, Pinning in type II superconductors, J. Low Temp. Phys. **34**, 409 (1979).

[39] A. B. Kolton, A. Rosso, and T. Giamarchi, Creep motion of an elastic string in a random potential, Phys. Rev. Lett. **94**, 047002 (2005).

[40] I. Culjak, D. Abram, T. Pribanic, H. Dzapo, and M. Cifrek, in *2012 Proceedings of the 35th International Convention MIPRO* (IEEE, Opatija, Croatia, 2012), p. 1725.